

Electronic landscape of the P-cluster of nitrogenase as revealed through many-electron quantum wavefunctions

Zhendong Li^{1*}, Sheng Guo¹, Qiming Sun¹, Garnet Kin-Lic Chan^{1*}

Division of Chemistry and Chemical Engineering, California Institute of Technology,
Pasadena, CA 91125, USA

*To whom correspondence should be addressed;

E-mail: zhendongli2008@gmail.com, gkc1000@gmail.com

The electronic structure of the nitrogenase metal cofactors is central to nitrogen fixation. However, the P-cluster and iron molybdenum cofactor, each containing eight irons, have resisted detailed characterization of their electronic properties. Through exhaustive many-electron wavefunction simulations enabled by new theoretical methods, we report on the low-energy electronic states of the P-cluster in three oxidation states. The energy scales of orbital and spin excitations overlap, yielding a dense spectrum with features we trace to the underlying atomic states and recouplings. The clusters exist in superpositions of spin configurations with non-classical spin correlations, complicating interpretation of magnetic spectroscopies, while the charges are mostly localized from reorganization of the cluster and its surroundings. Upon oxidation, the opening of the P-cluster significantly increases the density of states, which is intriguing given its proposed role in electron transfer. These results demonstrate that many-electron simulations stand to provide new insights into the electronic structure of the nitrogenase cofactors.

The Fe-S clusters of nitrogenase, namely, the $[\text{Fe}_4\text{S}_4]$ Fe-cluster of the Fe-protein, and the $[\text{Fe}_8\text{S}_7]$ P-cluster and $[\text{MoFe}_7\text{S}_9\text{C}]$ FeMo-cofactor of the MoFe protein, are the active sites for electron transfer and reduction in biological nitrogen fixation (1–4). The P-cluster and FeMo-cofactor, in particular, stand as peaks in the electronic complexity of enzymatic cofactors, with eight spin-coupled, open-shell, transition metal ions. Resolving their atomic and electronic structure has stood as a major challenge for experimental and theoretical spectroscopies. In the last decades, careful application of experimental techniques, including X-ray crystallography and spectroscopy, Mössbauer spectroscopy, and electron paramagnetic resonance (EPR), amongst others, has led to precise atomic structures, first for the Fe-cluster, followed by the P-cluster, and most recently, the FeMo-cofactor (5, 6). Like others, we have been working towards a complementary goal of determining the electronic structure of the three clusters at a detailed, many-electron, level. A few years ago, we reported an *ab initio* picture of the electronic states of the (4Fe-4S) Fe cluster that revealed a rich low-energy landscape (7), with a density and variety of states far greater than previously thought. In this article, we report on the electronic landscape of the P-cluster.

The P-cluster is thought to mediate electron transfer from the Fe-cluster to the FeMo-cofactor where nitrogen reduction occurs. The relevant charge states are considered to be the resting state P^{N} , the one-electron oxidized state P^{1+} , and the two-electron oxidized state P^{OX} (8, 9), although the recently proposed deficit spending mechanism (9, 10) postulates that only the P^{N} and P^{1+} states take part in electron transfer. X-ray crystallography reveals a structure consisting of an $[\text{Fe}_8\text{S}_7]$ core and two cubanes sharing a sulfur bridge. Under oxidation the cluster undergoes a large structural opening, driven by coordination first of Ser- β 188 to Fe4 in P^{1+} , followed by Cys- α 88 to Fe2 in P^{OX} (11, 12); the role of this structural opening in the mechanism of electron transfer is poorly understood. Fig. 1a highlights the redox-dependent structural rearrangements across P^{N} , P^{1+} , and P^{OX} .

While the atomic structure of the P-cluster is resolved, information on the electronic structure is fragmentary (see SM for a brief introduction). However, relating structure to chemical function requires to know the basic oxidation and spin states, and interpreting spectra, particularly in magnetic spectroscopies such as EPR, requires models of the low-energy, spin-coupled, many-electron quantum states, and their spin and charge distributions. Here, we describe the first *ab initio* calculations of the quantum states of the P-cluster at the many-electron level. By some measures, the electronic complexity of this system is greater than that of any other molecular problem studied with *ab initio* many-electron simulation. In particular, the low-lying electronic states of the P-cluster are more numerous, and the spectrum is denser, than what we previously encountered in the already challenging Fe-cluster. As a result, the energy resolution we can achieve (<3 kcal/mol in energy differences) does not fully resolve the precise ordering of all states. However, analogous to how an X-ray crystal structure at close to atomic-scale resolution displays the larger scale structural features of a protein, our current calculations reveal the larger scale features of the electronic landscape. In particular, we wish to understand how spin and charge is distributed in the P-cluster; how the individual moments combine to form the global spin state; what types of excitations appear at low energies; and the implications for spectroscopy and the function of the P-cluster in electron transfer. We will address these questions using new theoretical techniques and exhaustive simulations.

Theoretical strategy

We first recall why *ab initio* many electron simulation is necessary even to achieve a qualitatively correct description. One-electron computational models, such as provided by broken-symmetry density functional theory (BS-DFT) (13–16), are commonly applied with success to transition metal complexes. However, they encounter limitations when there are multiple open-shells with mixed valence character, as found in the P-cluster. This is because BS-DFT requires

a fixed spin configuration at each Fe center, and thus does not treat the spin-coupling between centers that produces the global electronic spin-state (with a well-defined spin quantum number) as a superposition of many different metal spin configurations. Instead, to handle this, BS-DFT is usually augmented by a model analysis, where a parametrized model spin-Hamiltonian is diagonalized to obtain the many-spin wavefunction (a simplification of the true many-electron state). However, as we determined in the $[\text{Fe}_4\text{S}_4]$ cluster (7), such model Hamiltonians do not properly account for the multiple d orbitals relevant to mixed valence metals, and thus miss many of the low-lying excited states, underestimating the spectral density in the $[\text{Fe}_4\text{S}_4]$ cluster by an order of magnitude or more. A complete picture can thus only be obtained when superpositions of both spin and orbital degrees of freedom are fully considered; this is what is provided by an *ab initio* many-electron simulation.

Solving the many-electron Schrödinger equation exactly for the full P-cluster is not currently possible. To obtain a tractable simulation, we instead solve the Schrödinger equation only within the space of the most important orbitals, a complete active space (CAS), and represent the wavefunction as a matrix product state (MPS) (17), the class of wavefunctions generated by the density matrix renormalization group (DMRG) (18, 19). In iron-sulfur clusters, the natural active space comprises the Fe $3d$ and S $3p$ (necessary for double exchange (20)) valence orbitals. However, even within the active space, and only counting configurations derived from ferric Fe $3d$ configurations, the number of relevant electron configurations is enormous, with as many $\sim 10^{22}$ relevant configurations for the $[\text{Fe}_8\text{S}_7]$ core. To tackle this, the MPS provides a compression of the wavefunction, controlled by single parameter D , the bond dimension. Simulating with an MPS with different finite D , followed by extrapolating $D \rightarrow \infty$, then yields an estimate of the exact solution in the active space.

We previously used such CAS DMRG simulations to correctly describe the electronic states of the Fe-cluster (7). However, there are additional complications in the P-cluster that require

special theoretical treatment, arising from the fact that the low-energy spectrum contains a large variety of qualitatively very different electronic states. As a result, the non-linear optimization of the wavefunction in the DMRG algorithm is easily trapped in local minima, preventing access to the full spectrum. To address this, we have designed a new theoretical procedure that combines the simple enumerability of BS-DFT solutions with the representational power of MPS. We first enumerate all low-lying BS-DFT states, each of which can be thought of as a simple, $D = 1$, MPS. From these electronic basins, we then apply spin-projection and increase the bond-dimension of the MPS to obtain a more flexible wavefunction that can properly capture the many-electron eigenstate. The procedure is outlined schematically in Fig. 1c and described in detail in the SM.

Using this procedure, we carried out calculations on structural models of the P^N , P^{1+} , P^{OX} clusters derived from the cofactor in *Azotobacter vinelandii* and its surrounding residues, as well as a synthetic model cluster (21) (Fig. 1a). The *ab initio* CAS DMRG calculations treated up to 120 electrons in 77 orbitals CAS(120e,77o). Further details are in the methods section as well as in the SM.

It is important to estimate the sources of theoretical uncertainty. There are multiple sources including the geometry and environment, basis sets, correlation treatments, and the convergence of the DMRG solutions. From a detailed analysis of these factors in smaller chemical analogs (see SM), we estimate the uncertainty in the relative energies of the low-lying states of interest (within ca. 10 kcal/mol of the ground state) at a fixed geometry to be less than 3 kcal/mol in most cases, stemming from the uncertainty in the basis set and correlation treatments (ca. 2 kcal/mol) as well as in the DMRG convergence (<0.8 kcal/mol, except for the uncertainty in the energy difference between the lowest P^{OX} $S = 3$ and $S = 4$ states, which is about 2.8 kcal/mol). This level of accuracy means that the low energy states we observe will remain low energy states in more exact calculations, although it does not resolve all state orderings due to

the high density of the spectrum. Consequently, our objective is to address qualitative questions regarding the structure of the low energy spectrum. The electronic landscape we uncover serves as a zeroth order approximation for more elaborate calculations in the future.

Results

Families of low-lying states in the P-cluster

Before proceeding to the computational results, we briefly present a framework to understand the electronic landscape (Fig. 2). The low energy electronic states of the P-cluster (i.e. states within a few kcal/mol of the ground-state) arise from different ways to assemble the global state from individual Fe configurations. The relevant Fe oxidation states lie between Fe(II), Fe(III), with corresponding spins between $S = 2$ and $S = 5/2$. The orbital configurations arise from an approximately tetrahedral, weak ligand field from the sulfurs around each metal, with distortions that further split the t_2 and e_g orbitals (22).

Since the P-cluster consists of conjoined cubanes, the $[\text{Fe}_4\text{S}_4]$ cubane is a natural intermediate unit to understand the electronic structure. Each cubane itself has a large number of states at low energy, arising from (1) local ligand-field excitations of Fe(II)/Fe(III) ions, (2) double exchange hopping between all the Fe $3d$ orbitals, and (3) Heisenberg-like ladders of spin-coupling in Fe-dimers (and dimers of such dimers). Double exchange couples the spin state and charge delocalization in the cubane (23).

The states of the two cubanes are further electronically coupled across the bridging sulfur to produce the global P-cluster state. Note that the coupling not only gives rise to families of states (such as Heisenberg ladders generated from the two cubane total spins) but also allows for different types of states on the same cubane to mix. This latter case gives a true many-electron “multi-configurational” superposition, as one cannot assign a single spin configuration (i.e. configuration state function) to the left or right cubane. Instead, the global state needs to be

described by a superposition of couplings of various different left and right cubane states, and we can only refer to the average cubane spins (S_{eff} or S_L, S_R), computed as expectation values, for the cubanes.

From the above scheme, we can group the low-energy states into 3 families (Fig. 2). The first are (A) spin isomers, which have the same total spin as the ground-state, but differ by local reorientations of the spins and their couplings; these are conveniently discussed in terms of changes in the underlying cubane states; (B) orbital excitations, where electron configurations of the ions change (e.g. in ligand field excitations); and (C) global spin excitations, where the cubanes recouple into a different spin state from the ground-state. Excitations in class A and C are true many-electron excitations and cannot be fully described within BS-DFT, while excitations in class B are missed in typical model Hamiltonians, which do not contain all $3d$ orbital degrees of freedom. The energy scales associated with A are the exchange and double-exchange energies within a cubane; that associated with B is the ligand field splittings; and that associated with C is the exchange and double exchange between the cubanes. As we shall see, these energy scales all overlap in the low-energy states of the P-cluster.

The P^N cluster and its synthetic model

Ground states. We start with the ground states of P^N and a synthetic model cluster with a similar core geometry (Fig. 3). Consistent with Mössbauer and EPR spectra, we find the P^N ground state to be a singlet ($S = 0$) with all ferrous irons. The cubanes assume $S = 4$ states ($S_{\text{eff}} \approx 3.7$) corresponding to the $S = -2 + (2 + 2 + 2) = 4$ (3:1) coupling scheme between the terminal and other three Fe's. We note that this cubane electronic motif is also found in the $[\text{Fe}_4\text{S}_4]^0$ cluster in the super-reduced iron protein (24, 25), and cubanes in similar electronic states have been used to assemble the P-cluster in a non-enzymatic synthesis (26).

In contrast to the natural P^N cluster, the synthetic model also has an $S = 0$ ground-state,

but with Fe oxidation states close to $6\text{Fe(II)}2\text{Fe(III)}$. However, the cubane electronic states are related to those in the P^{N} cluster, with the charges localized on the terminal Fe's, and a similar 3:1 coupling pattern yielding $S = 7/2$ cubanes. Note that the driving force for charge localization does not come solely from the terminal ligands, but also has a small spin-coupling contribution: a delocalized cubane charge is typically associated with an $S = 1/2$ cubane (23), but the $S = 7/2$ cubane (with localized charge) maximizes the number of antiferromagnetic (AFM) Fe pairs. In particular, in the $S = 7/2$ cubane, there are 9 (intercubane) + 6 (intracubane) = 15 AFM pairs, while for the $S = 1/2$ cubane, there are 5 (intercubane) + 8 (intracubane) = 13 AFM pairs.

Excited states. All three classes of excited states are found in the low-energy (< 8 kcal/mol) spectrum (Figs. 3a, 3b). Global recoupling of the $S = 4$ (P^{N}) (model: $S = 7/2$) cubanes into an overall triplet ($S = 1$) state occurs at 0.6 kcal/mol (P^{N}) (model: 1.1 kcal/mol) above the ground-state. This leads to an inter-cubane Heisenberg ladder of states (class C excitations) with an effective $J \approx 200\text{cm}^{-1}$. Intracubane spin (class A) excitations that modify the 3:1 coupling on one of the cubanes occur at higher energies (e.g. starting at ~ 6 kcal/mol) reflecting the larger intracubane effective J . Finally, some ligand-field excitations from partially split e and t_2 orbitals appear at very low energy and on a similar scale to the spin excitations, with the lowest $d \rightarrow d$ transition in Fe8(II) appearing at about 2 kcal/mol (ca. 700cm^{-1}). Both localized ligand field excitations, as well as delocalized linear combinations of $d \rightarrow d$ transitions similar to those in bulk FeS, can be found.

The oxidized P-clusters: P^{1+} and P^{OX}

In the P^{1+} and P^{OX} clusters, the opening of the core weakens the coupling between the cubanes. Together with the multiple Fe oxidation states and overall non-singlet ground-state, this gives rise to a greater degeneracy of states at low energy and a more complicated spectrum. The

sets of P^{1+} and P^{OX} states can be related both to each other and to those of P^N , and these relationships are illustrated in Fig. 5.

$S = 1/2$ and $S = 5/2$ ground-states of P^{1+} . EPR suggests that both $S = 1/2$ and $S = 5/2$ are potential ground state spins for P^{1+} (27). We find the $S = 5/2$ ground state to be slightly lower in energy than the $S = 1/2$ state (-2.7 kcal/mol) but within the range of theoretical uncertainty. In both the $S = 1/2$ and $S = 5/2$ ground-states, the charge is localized, with oxidation mainly on Fe4, which coordinates to the oxygen in Ser-188 in conjunction with the structural opening. Additionally, the irons in the right cubane are overall more reduced than the irons in the left cubane (shading in Figs. 4a, 4b) likely due to the compressed cubane structure and closer proximity of the ligands, furthering the charge imbalance between the cubanes. The spin structure of the P^{1+} cluster ground-state is complicated (Figs. 4a, 4b): in the $S = 1/2$ (A1) ground-state, the left cubane consists of a ferromagnetically coupled (dimer of $S \approx 4$ dimers) $S_L = 4.1$ state, with the right cubane in a similar $S_R \approx 4$, 3:1 coupled state as seen in the P^N cluster. In the $S = 5/2$ (A1) ground-state, the left cubane consists of the same dimer of dimers, but now coupled antiferromagnetically into a low spin $S_L = 0.9$ state, with the right cubane in a superposition of cubane states with $S_R = 2.3$, see Fig. 5.

$S = 3$ and $S = 4$ ground-states of P^{OX} . Experimentally, the ground-state spin of the P^{OX} cluster is not known with certainty (28), and both $S = 3$ and $S = 4$ spin states can be identified in related P-clusters (29), such as in *Gluconacetobacter diazotrophicus*. For $S = 4$ we find that the ground-state is close to degenerate (states A1, A2), while the $S = 3$ (A1) ground state lies above the $S = 4$ ground-state by 1.4 kcal/mol, but well within the theoretical uncertainty. In both spin states, Fe2 and Fe4 are the principal sites of oxidation, with largely localized charges correlated with ligating to hard ligands (O and N) and the structural opening, with some residual ferric character on the other Fe's in the left cubane (shading in Figs. 4c, 4d). The opening of the left cubane resembles that seen in isolated cubanes under oxidation, such as the conforma-

tional change of the $[\text{Fe}_4\text{S}_3]$ cluster upon oxidation in oxygen-tolerant membrane-bound $[\text{NiFe}]$ hydrogenases (30–33). Unlike in the P^{N} cluster, there is no simple classical picture of the spin-coupling in P^{OX} ; each state is spin-canted (34) and involves a linear combination of multiple spin coupling schemes.

Excited states of P^{1+} and P^{OX} . As shown in Figs. 4c, 4d, similarly to in P^{N} , we find localized and delocalized low-energy $d \rightarrow d$ ligand field transitions (class B excitations). The main difference between the P^{1+} and P^{OX} low energy landscape from that of P^{N} arises from the spin isomers (class A and C excitations). Whereas in the P^{N} cluster we find that there is some separation in energy scales between inter-(small) and intra-(large) cluster spin reorganizations, in the P^{1+} and P^{OX} clusters both energy scales are comparably small, leading to a higher density of states. Thus while our procedure identifies only a spin-coupling pattern of the P^{N} cluster ($S = 0$) below 5 kcal/mol, in the P^{1+} cluster we find 2 and in the P^{OX} cluster we find 4. In particular, the opening of the left cubane and additional charges in P^{1+} and P^{OX} introduces new left cubane coupling patterns (2:2 or dimer of dimers) at comparable energies to the 3:1 spin-coupled state in P^{N} . The dimer of dimers spin coupling motif leads to an approximate spin ladder in the left cubane ($S_L \approx 0.8, 1.6, 2.4, 3.3, 4.1$) that can be seen in the different low energy P-cluster states (see left panel of Fig. 5). The fractional S_L is due to charge delocalization (see Fe in dark red in the inset of Fig. 4). The right cubane states can be found in various combinations of 2:2 and 3:1 spin-coupling patterns. Fig. 5 shows how these different excited states arise from the underlying cubane spin states in the P-clusters.

Discussion

The cluster states can display non-classical spin correlations. From a theoretical perspective, it is useful to highlight the electronic features of the states we observe beyond that described in standard treatments. For example, even though the BS-DFT spin densities would be qualita-

tively wrong in all states here (e.g. giving non-vanishing spin density in the $S = 0$ states) the *relative* orientation of the iron spins (a so-called “classical” spin correlation pattern) could in principle still resemble that in the many-electron state. In some states, such as the $S = 0$ ground state (A1) of P^N and $S = 1/2$ A2 state of P^{1+} , this is indeed the case. However, a succinct example of a state with non-classical spin correlations is the $S = 3$ ground state of P^{OX} (see Fig. 4c) which has 6 spin-up and 2 spin-down Fe’s. Within BS-DFT, such a spin distribution can *only* arise for an $S > 3$ state, leading to an inconsistency. Similarly, compared to a traditional model Hamiltonian analysis, the cubane effective spins S_L and S_R away from integer or half-integer cannot be captured by a simple spin-coupling scheme. These kinds of non-classical spin correlations clearly affect the interpretation of magnetic spectroscopies (see below), which have previously relied on BS-DFT or a single spin-coupling scheme. It may also have implications for the electronic structure of the FeMo-cofactor, where analysis of the $S = 3/2$ ground state spin distribution has so far exclusively relied on BS-DFT (35–39).

The oxidized clusters contain localized charges. Despite the multiple metal centers, in P^{1+} and P^{OX} the charges are strongly localized and distributed asymmetrically between the cubanes. This is consistent with strong coupling to the ligands, a polaronic effect, and is reflected in the large geometric rearrangements of the cluster. We note that localized charge distributions have also been observed recently in FeMo-cofactor (40). This localization may be related to controllability of the density of states (see below).

Energy scales of spin and electronic excitations are comparable. While ligand field splitting and exchange effects are usually associated with different energy scales, both spin and orbital excitations are found at low energies in the P-cluster, especially in P^{1+} and P^{OX} . Spectroscopically, this means that apparently local magnetic responses need not arise from spin localisation. For example, recent MCD measurements found similar spectral features in P^{1+} and the $[Fe_4S_4]^+$ cubane (41), which was interpreted as meaning that the spin density in P^{1+} is localized to a

single cubane. However, as expected for a non-singlet ground-state, the spin density in P^{1+} is actually distributed across *both* cubanes. Instead, the similarity between P^{1+} and the $[\text{Fe}_4\text{S}_4]^+$ cubane MCD spectrum is more naturally explained in terms of the localized nature of the cubane one-electron excitations (class B excitations), as evidenced by the ligand field excitations, which are also probed by the MCD response.

Hyperfine coupling analysis. Using spin distributions consistent with a many-electron wavefunction representation of the states, we can attempt to reinterpret hyperfine coupling parameters using a model previously developed in (42, 43). In P^{OX} , hyperfine coupling parameters have been reported for some time, but have previously been analyzed only in terms of spin distributions consistent with a single configuration state function description (42). Note that the parameters are themselves obtained by fitting and are thus uncertain, but we can compare at least the relative signs and magnitudes of the internal magnetic field H_{int} to the local spin S_{Fe}^z for qualitative insight. As shown in Table 1, the hyperfine parameters have a 6:2 sign pattern similar to that of the $S = 3$ ground state spin distribution (that arises from the multi-configurational superposition) whereas the lowest $S = 4$ state has a 5:3 sign pattern. Unfortunately, the 5:3 pattern was not considered in earlier experimental fits (44), and thus cannot be compared on an equivalent footing. Out of the two 6:2 patterns, the small $S_{\text{Fe}}^z = 0.47$ for Fe2 (ligated with the amide-N) correlates with the small hyperfine parameter no. 4, while the increased charge on Fe2, which thus has more ferric character compared to the other sites, is consistent with the isomer shift of $\delta = 0.25$ mm/s for the same iron (no. 4). The P^{OX} $S = 3$ ground state thus correlates best with the experimentally reported hyperfine parameters.

The density of states increases significantly upon oxidation. Near the ground-state, the density of states in P^{1+} and P^{OX} is much higher than that of P^{N} , the physical origin of which can be traced to the opening of the cluster. This is intriguing in the context of the role of P-cluster in the electron transfer process. In the proposed deficit spending mechanism (9, 10), the first step is

Table 1: Comparison of the experimental hyperfine parameters (internal magnetic fields H_{int} in kG, quadrupole splittings ΔE_Q in mm/s, isomer shifts δ in mm/s) from Ref. (44) with the computed local charges N_{Fe} and spin projections S_{Fe}^z for the lowest $S = 3$ and $S = 4$ states of the P^{OX} cluster of *Azotobacter vinelandii*. The values of N_{Fe} for ground states of P^{N} and the synthetic model are listed as references.

no.	Expt. (44)			atom ^a	$\text{P}^{\text{OX}} (S = 3)$		$\text{P}^{\text{OX}} (S = 4)$		N_{Fe}	
	H_{int}	ΔE_Q	δ		N_{Fe}	S_{Fe}^z	N_{Fe}	S_{Fe}^z	P^{N}	Syn
1	-287	-1.40	0.56	Fe1	6.24	0.52	6.24	-0.52	6.33	6.15
2	-237	+1.53	0.64	Fe2	6.15	0.47	6.15	0.44	6.46	6.32
3	-245	+0.57	0.40	Fe3	6.22	0.55	6.23	0.43	6.38	6.30
4	-151	+0.60	0.25	Fe4	6.07	1.04	6.08	-0.58	6.35	6.44
5	-259	+1.26	0.48	Fe5	6.34	-1.24	6.32	1.64	6.51	6.30
6	-237	-0.72	0.49	Fe6	6.41	1.42	6.40	1.66	6.48	6.32
7	201	+3.20	0.65	Fe7	6.33	1.55	6.28	1.74	6.33	6.45
8	223	+2.30	0.68	Fe8	6.18	-1.40	6.26	-1.33	6.32	6.15

^a The index does not correspond to the no. in the first column.

a slow electron transfer from the P^{N} cluster to the FeMo-cofactor, followed by a fast refilling of the oxidized P cluster from the Fe cluster. The higher density of states in P^{1+} is thus consistent with the fast refilling.

Controllable states hypothesis. The P-cluster has a large density of states, a factor that affects electron transfer. There are in principle two ways to obtain such a large number of states. The first is to create a (partially filled) metallic band from strong orbital overlap. The second is to have a large number of weakly coupled, localized atomic orbitals at different energies, arising from different local environments. The latter is much closer to the situation in the P-cluster (and Fe-S clusters in general). We suggest this second scenario, which gives rise to complex spin couplings from the many-electron recoupling of local states, could be favoured in the nitrogenase clusters because it provides for greater controllability. The local origin of the states means that local changes in geometry (or environment, such as ligation) can be used to modify the density of states, as we see in the coupling of the low-energy landscape to the opening of the $[\text{Fe}_8\text{S}_7]$ core structure as one progresses from P^{N} to P^{1+} to P^{OX} (Fig. 5).

Conclusions

In summary, we have shown that we can now access the electronic structure of the P-cluster of nitrogenase at the level of many-electron wavefunction simulations that can qualitatively capture the richness of the low energy landscape. We report on a plethora of low-energy states across the P^N , P^{1+} , and P^{OX} clusters and their composition in terms of the local atomic configurations, spins, and spin-couplings. The many-electron nature of the states manifests in unusual spin distributions that are not contained in simpler broken-symmetry analyses, and energy scales of spin and charge excitations that overlap. Together these imply a non-trivial interpretation of magnetic spectroscopies. The opening of the cluster leads to an increase in the low-energy density of states, that is intriguing in the context of the proposed deficit spending mechanism, and the local nature of the charges may be essential for local tuning and control. Our work forms an element in resolving the story of the nitrogenase enzyme, where many-electron wavefunction theory may now be used to access structures at the electronic level, just as crystallography has advanced our understanding at the atomic level.

Author contributions

Z.L. and G.K.C. designed the study and wrote the manuscript. Z.L. performed the calculations, supported by US nsf-che 1665333. S.G. contributed to interfacing SP-MPS to SA-MPS used in the BLOCK code, supported by US nsf-ssi 1657286. Q.S. contributed to interfacing the PYSCF code with COSMO, supported by US nsf-ssi 1657286. All authors contributed to the discussion of the results.

Methods

Starting from the P cluster structural models (see SM), we embedded all calculations in a dielectric with $\epsilon = 4.0$ to mimic the remaining protein environment. For the 4 different model P clusters, we constructed the CAS using all Fe $3d$ and S $3p$ orbitals of the $[\text{Fe}_8\text{S}_7]$ core as well as the bonding orbitals with other ligands. This came to 108 electrons in 71 orbitals (denoted as CAS(108e,71o)) for the synthetic cluster; CAS(114e,73o) for P^{N} , CAS(117e,75o) for P^{1+} , and CAS(120e,77o) for P^{OX} , respectively; the size of the underlying many-electron Hilbert spaces range from 10^{31} to 10^{33} (Table S1). Note that the different active spaces (arising from the change in ligation) for the different P-cluster states means that we cannot directly compare energies across different clusters; redox potentials will be the subject of future studies. The initial BS basins used to initialize the DMRG calculations for each complex are summarized in Fig. 1b. In total, we examined 20 basins for the synthetic cluster ($S = 0$), 35 for P^{N} ($S = 0$), 70 for P^{1+} ($S = 1/2$ and $S = 5/2$), and 152 for P^{OX} ($S = 3$ and $S = 4$). To understand how the energetic landscape arises, we computed local observables such as the charge $N_A = \langle \hat{N}_A \rangle$ and local spin projection $S_A^z = \langle \hat{S}_A^z \rangle$, as well as Fe-Fe spin-spin correlation functions $\langle \vec{S}_A \cdot \vec{S}_B \rangle$ (see SM). From these, we deduced how the global states appear from recoupling local orbital and spin degrees of freedom, and the relationships between the electronic states in P^{N} , P^{1+} , and P^{OX} . The spin-projected and spin-adapted DMRG calculations were carried out with the codes developed in Refs. (45) and (46), respectively. Further discussions of the geometry, active spaces, accuracy, convergence, analysis, and other aspects, are in the SM.

References and Notes

1. H. Beinert, R. H. Holm, E. Münck, *Science* **277**, 653 (1997).
2. J. B. Howard, D. C. Rees, *Chemical reviews* **96**, 2965 (1996).
3. D. C. Rees, J. B. Howard, *Science* **300**, 929 (2003).
4. B. M. Hoffman, D. Lukoyanov, Z.-Y. Yang, D. R. Dean, L. C. Seefeldt, *Chemical reviews* **114**, 4041 (2014).
5. T. Spatzal, *et al.*, *Science* **334**, 940 (2011).
6. K. M. Lancaster, *et al.*, *Science* **334**, 974 (2011).
7. S. Sharma, K. Sivalingam, F. Neese, G. K.-L. Chan, *Nature Chem.* **6**, 927 (2014).
8. J. M. Chan, J. Christiansen, D. R. Dean, L. C. Seefeldt, *Biochemistry* **38**, 5779 (1999).
9. K. Danyal, D. R. Dean, B. M. Hoffman, L. C. Seefeldt, *Biochemistry* **50**, 9255 (2011).
10. L. C. Seefeldt, *et al.*, *Accounts of chemical research* **51**, 2179 (2018).
11. J. W. Peters, *et al.*, *Biochemistry* **36**, 1181 (1997).
12. S. M. Keable, *et al.*, *Journal of Biological Chemistry* **293**, 9629 (2018).
13. L. Noodleman, J. G. Norman Jr, J. H. Osborne, A. Aizman, D. A. Case, *Journal of the American Chemical Society* **107**, 3418 (1985).
14. L. Noodleman, E. R. Davidson, *Chemical physics* **109**, 131 (1986).
15. K. Yamaguchi, T. Fueno, N. Ueyama, A. Nakamura, M. Ozaki, *Chemical physics letters* **164**, 210 (1989).

16. M. Shoji, *et al.*, *International journal of quantum chemistry* **106**, 3288 (2006).
17. U. Schollwöck, *Ann. Phys.* **326**, 96 (2011).
18. S. R. White, R. L. Martin, *J. Chem. Phys.* **110**, 4127 (1999).
19. G. K.-L. Chan, S. Sharma, *Annu. Rev. Phys. Chem.* **62**, 465 (2011).
20. P. W. Anderson, H. Hasegawa, *Physical Review* **100**, 675 (1955).
21. Y. Ohki, Y. Sunada, M. Honda, M. Katada, K. Tatsumi, *Journal of the American Chemical Society* **125**, 4052 (2003).
22. D. Coucouvanis, *et al.*, *Journal of the American Chemical Society* **103**, 3350 (1981).
23. L. Noodleman, *Inorganic Chemistry* **30**, 246 (1991).
24. G. D. Watt, K. Reddy, *Journal of inorganic biochemistry* **53**, 281 (1994).
25. H. C. Angove, S. J. Yoo, B. K. Burgess, E. Münck, *Journal of the American Chemical Society* **119**, 8730 (1997).
26. K. Rupnik, *et al.*, *Biochemistry* **53**, 1108 (2014).
27. R. C. Tittsworth, B. J. Hales, *Journal of the American Chemical Society* **115**, 9763 (1993).
28. K. K. Surerus, *et al.*, *Journal of the American Chemical Society* **114**, 8579 (1992).
29. C. P. Owens, F. E. Katz, C. H. Carter, V. F. Oswald, F. A. Tezcan, *Journal of the American Chemical Society* **138**, 10124 (2016).
30. Y. Shomura, K.-S. Yoon, H. Nishihara, Y. Higuchi, *Nature* **479**, 253 (2011).
31. J. Fritsch, *et al.*, *Nature* **479**, 249 (2011).

32. A. Volbeda, *et al.*, *Proceedings of the National Academy of Sciences* (2012).
33. S. G. Tabrizi, V. Pelmeshnikov, L. Noodleman, M. Kaupp, *Journal of chemical theory and computation* **12**, 174 (2015).
34. L. Noodleman, W.-G. Han, *JBIC Journal of Biological Inorganic Chemistry* **11**, 674 (2006).
35. T. Lovell, J. Li, T. Liu, D. A. Case, L. Noodleman, *Journal of the American Chemical Society* **123**, 12392 (2001).
36. I. Dance, *Inorganic chemistry* **50**, 178 (2010).
37. P. E. Siegbahn, *Journal of the American Chemical Society* **138**, 10485 (2016).
38. R. Bjornsson, F. Neese, S. DeBeer, *Inorganic chemistry* **56**, 1470 (2017).
39. L. Cao, U. Ryde, *International Journal of Quantum Chemistry* **118**, e25627 (2018).
40. T. Spatzal, *et al.*, *Nature communications* **7**, 10902 (2016).
41. K. Rupnik, *et al.*, *Journal of the American Chemical Society* **134**, 13749 (2012).
42. J.-M. Mouesca, L. Noodleman, D. Case, *Inorganic Chemistry* **33**, 4819 (1994).
43. J.-M. Mouesca, L. Noodleman, D. Case, B. Lamotte, *Inorganic Chemistry* **34**, 4347 (1995).
44. B. Huynh, *et al.*, *Biochimica et Biophysica Acta (BBA)-Protein Structure* **623**, 124 (1980).
45. Z. Li, G. K.-L. Chan, *Journal of Chemical Theory and Computation* **13**, 2681 (2017).
46. S. Sharma, G. K.-L. Chan, *J. Chem. Phys.* **136**, 124121 (2012).

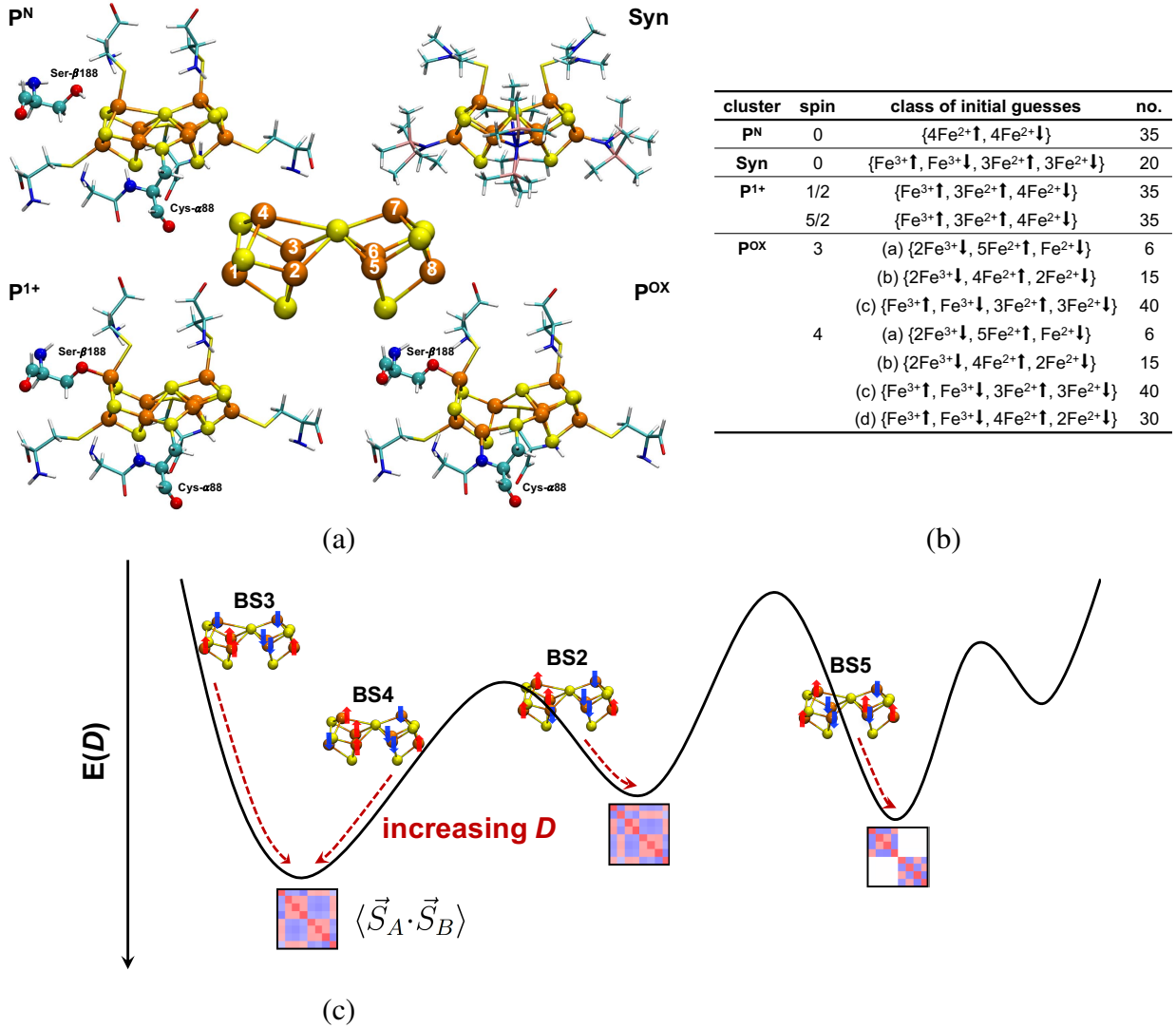


Figure 1: (a) [Fe₈S₇] P-cluster models in the present study (PDB ID: 3MIN for P^N, 6CDK for P¹⁺, and 2MIN for P^{OX}, and the synthetic analog of the P^N cluster in Ref. (21)). The labels in the central figure index the Fe atoms in the discussion. The redox-dependent structural rearrangement across P^N, P¹⁺, and P^{OX} involving Ser-β188 and Cys-α88 is highlighted. Color legend: Fe, orange; S, yellow; C, cyan; O, red; N, blue; H, white; Si, pink. (b) Table of initial guesses (broken-symmetry product states) obtained by distributing different iron states across the eight Fe atoms. (c) Schematic illustration of the change of energy in the DMRG optimization process as a function of bond dimension (D) starting from different broken-symmetry initial guesses. The local minima in the parameter space represent (approximate) eigenstates of the many-electron Schrödinger equation within the active space. They are characterized by the spin-spin correlation functions $\langle \vec{S}_A \cdot \vec{S}_B \rangle$ among eight irons (red: positive, blue: negative) shown by the square graphs.

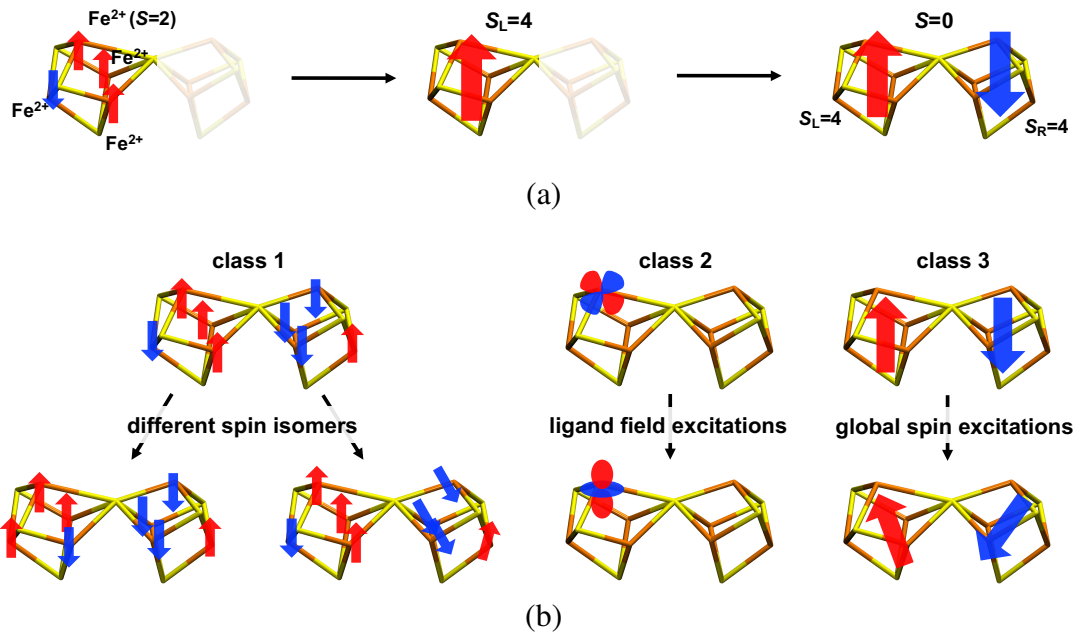


Figure 2: (a) Illustration of the coupling of local states of Fe^{2+} into local cubane states ($S_L = 4$) and finally into the global $S = 0$ ground state of P^N . (b) Schematic of typical excitations. class A: spin isomers with the same spin but differ in the spin-couplings; class B: ligand field (local orbital) excitations; class C: global spin excitations that changes the global spins but without altering the local cubane states.

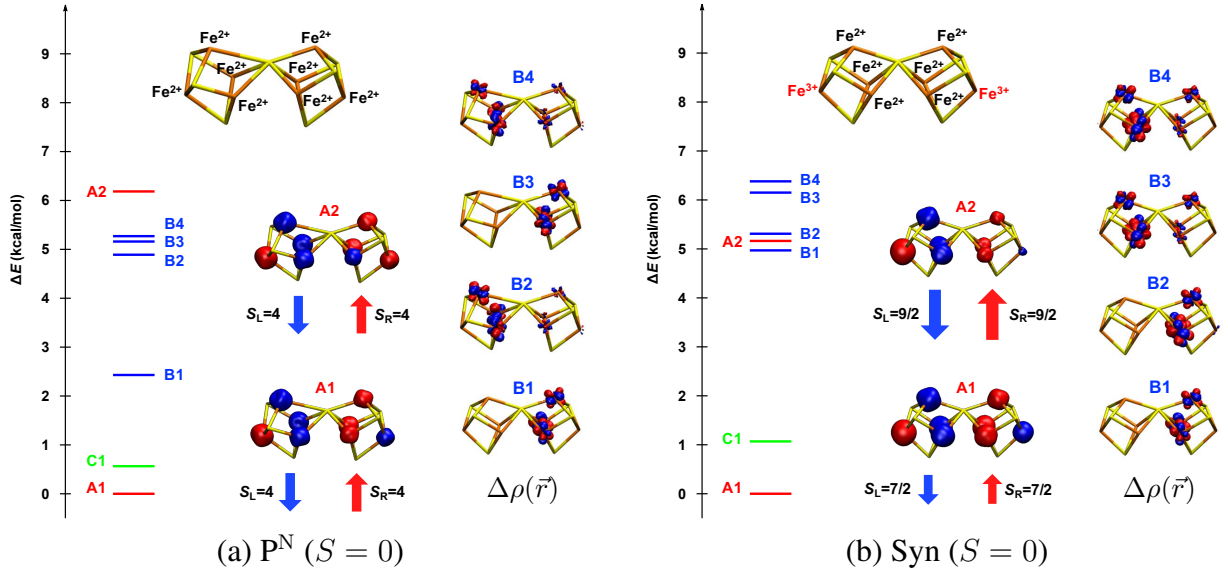


Figure 3: States of the (a) P^N and (b) synthetic cluster. Left panel: extrapolated relative energies ΔE (kcal/mol) for spin isomers (red) and estimated energies for the B1-B4 states via a state-averaged DMRG calculation ($D = 3000$) starting from the converged ground state. Inset: assigned formal oxidation states for the ground state based on local charge analysis. Middle panel: spin-coupling patterns of states A1 and A2 revealed by the spin-spin correlation density functions $\sigma_A(\vec{r}) = \langle \vec{S}_A \cdot \sum_B \vec{S}_B(\vec{r}) \rangle$ with $A=\text{Fe1}$ for the first iron of these two spin isomers. A schematic representation of the spin-coupling scheme by a 'classical' AFM coupling between two cubanes are shown below. Right panel: density differences $\Delta\rho(\vec{r})$ of B1-B4 states with respect to the ground state density.

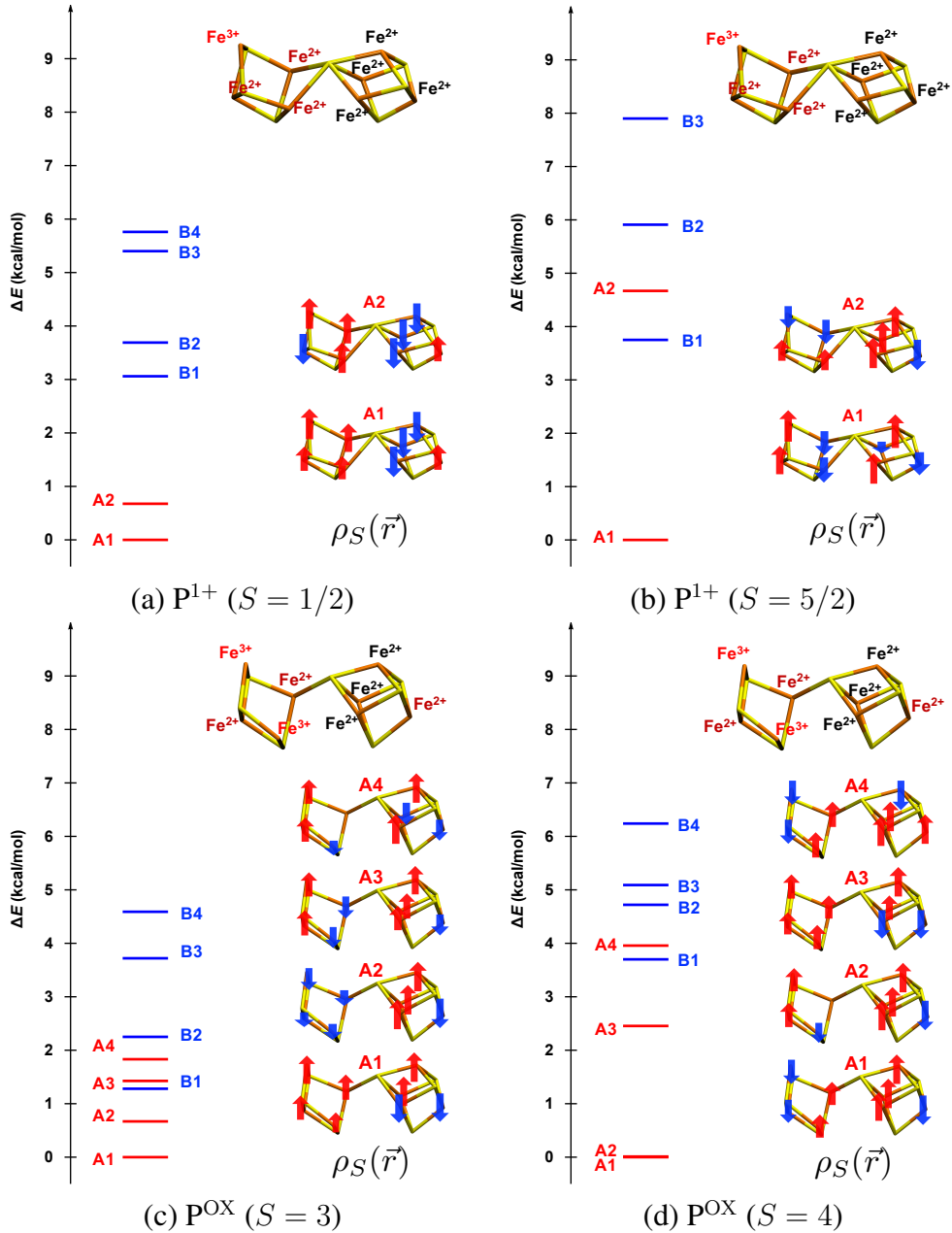


Figure 4: States of the oxidized P-clusters: (a) P^{1+} with $S = 1/2$, (b) P^{1+} with $S = 5/2$, (c) P^{OX} with $S = 3$, (d) P^{OX} with $S = 4$. Left panel: see text in Fig. 3. The lowest $S = 5/2$ state of P^{1+} is lower than the lowest $S = 1/2$ state by -2.7 kcal/mol computed with extrapolated energies, while the lowest $S = 4$ state of P^{OX} is lower than the lowest $S = 3$ state by -1.4 kcal/mol computed with extrapolated energies. Inset: assigned formal oxidation states for the ground state based on local charge analysis. Fe^{2+} symbols in dark red indicate that the irons have ferric character due to charge delocalization as compared to other ferrous irons in black. Right panel: schematic representation of the spin-density $\rho_S(\vec{r})$ of the lowest spin-isomers.

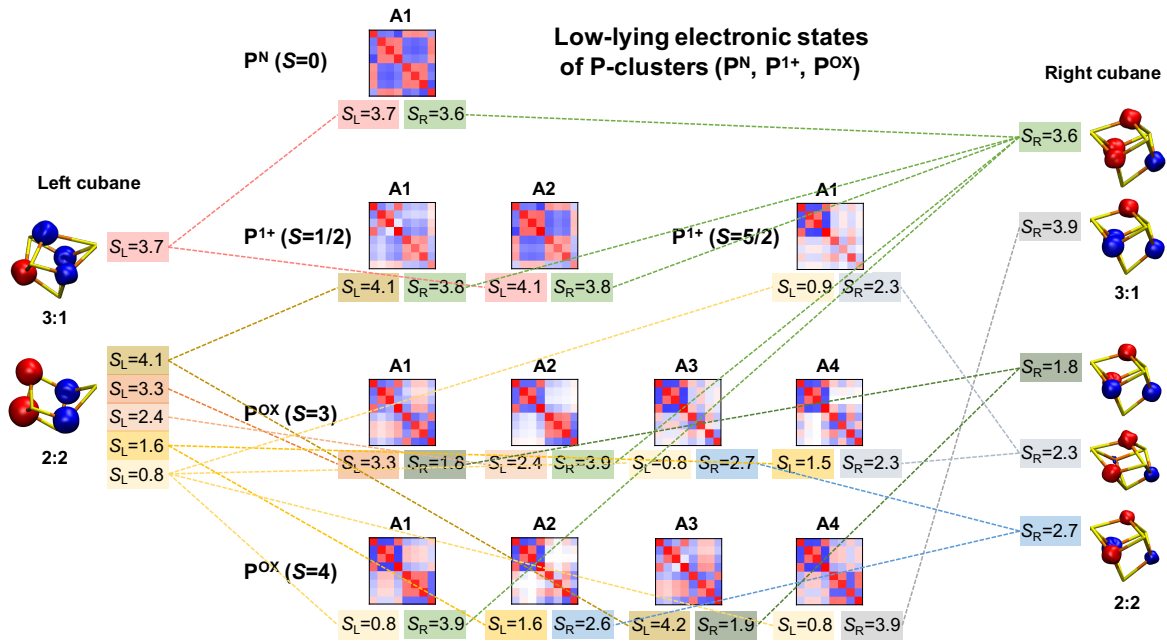


Figure 5: Relationships between spin-isomers in low-lying electronic states of the P-clusters, which unravel the evolution of local (left or right) cubane states upon oxidations. The cubane states sharing the same color are basically the same spin state. Square graph: Spin-spin correlation functions $\langle \vec{S}_A \cdot \vec{S}_B \rangle$ among eight irons (red: positive, blue: negative). The effective spins of the left cubane S_L and the right cubane S_R are computed for the irons on the left and right cubanes, respectively.